Ambient noise tomography across the Cascadia subduction zone using dense linear seismic arrays and double beamforming

Yadong Wang [1], Fan-Chi Lin[1] and Kevin M. Ward[1,2]

[1]*Department of Geology and Geophysics, The University of Utah, Salt Lake City, UT* 84112, *USA. E-mail: yadongwang1991@gmail.com*
[2]*Department of Geology and Geological Engineering, South Dakota School of Mines & Technology, Rapid City, SD* 57701, *USA*

SUMMARY
In the summer of 2017, we deployed 174 three-component nodal geophones along a 130 km west–east line across the central Oregon forearc lasting about 40 d. Our goal was to evaluate the possibility of imaging the lithospheric structure in detail with a dense but short-duration sampling of passive seismic signals. In this study, we used passive recordings from the nodal array and the previous CASC93 broad-band array along the same line to calculate noise cross-correlations. Fundamental Rayleigh wave signals were observed in the cross-correlations between 3 and 15 s period. To enhance the signal and simultaneously measure the phase velocity, we employed a double beamforming method. At each period and location, a source beam and a receiver beam were selected and the cross-correlations between the two were shifted and stacked based on the presumed local velocities. A 2-D grid search was then used to find the best velocities at the source and receiver location. Multiple velocity measurements were obtained at each location by using different source and receiver pairs, and the final velocity and uncertainty at each location were determined using the mean and the standard deviation of the mean. All available phase velocities across the profile were then used to invert for a 2-D shear wave crustal velocity model. Well resolved shallow slow velocity anomalies are observed corresponding to the sediments within the Willamette Valley, and fast velocity anomalies are observed in the mid-to-lower crust likely associated with the Siletzia terrane. We demonstrate that the ambient noise double beamforming method is an effective tool to image detailed lithospheric structures across a dense and large-scale (>100 km) temporary seismic array.

Key words: Crustal imaging; Seismic interferometry; Seismic noise; Seismic tomography; Surface waves and free oscillations.

1 INTRODUCTION AND TECTONIC BACKGROUND

Surface wave tomography is one of the main tools used to image the shallow earth structure. Traditional earthquake-based surface wave tomography usually focuses on long period signals that are mostly sensitive to upper-mantle structures (e.g. Friederich 1998; Ritzwoller & Levshin 1998; Levshin *et al.* 2001; Ritzwoller *et al.* 2002; Trampert & Woodhouse 2003; Levshin *et al.* 2005; Prindle & Tanimoto 2006; Adams *et al.* 2012), while ambient-noise-tomography extends the usable signal to shorter periods where detailed crustal structure can be imaged with data from continental, regional or local seismic arrays (e.g. Shapiro *et al.* 2005; Yao *et al.* 2008; Lin *et al.* 2007, 2008, 2013; Ward *et al.* 2013, Ekström 2014; Ward 2015; Zigone *et al.* 2015; Roux *et al.* 2016; Wang *et al.* 2017). While broad-band instruments are often used to study the continental to

regional lithospheric structure, recent studies demonstrate that inexpensive and easy-to-deploy nodal geophone instruments can record passive seismic signals below the instruments corner frequency (i.e. 10 or 5 Hz; Lin *et al.* 2013; Wang *et al.* 2017; Ward & Lin 2017).

To evaluate the possibility of studying regional scale tectonic structure based on a temporary large-N nodal array, a dense three-component 5 Hz geophone linear array (ZO2017) was deployed in central Oregon (Fig. 1) that closely followed the previous Cascadia 1993–94 (CASC93) broad-band deployment. The CASC93 array has been widely used to study structure of the Cascadia subduction zone. For example, Bostock *et al.* (2002) found low seismic velocities related to an inverted continental Moho using the converted teleseismic waves. Receiver function analysis from teleseismic events have been used to study the deep crustal fracture zones in the Cascadia forearc (Audet *et al.* 2010) and to constrain the slab morphology (Tauzin *et al.* 2017). While the primary goal of our experiment was to assess the feasibility of studying subduction zone
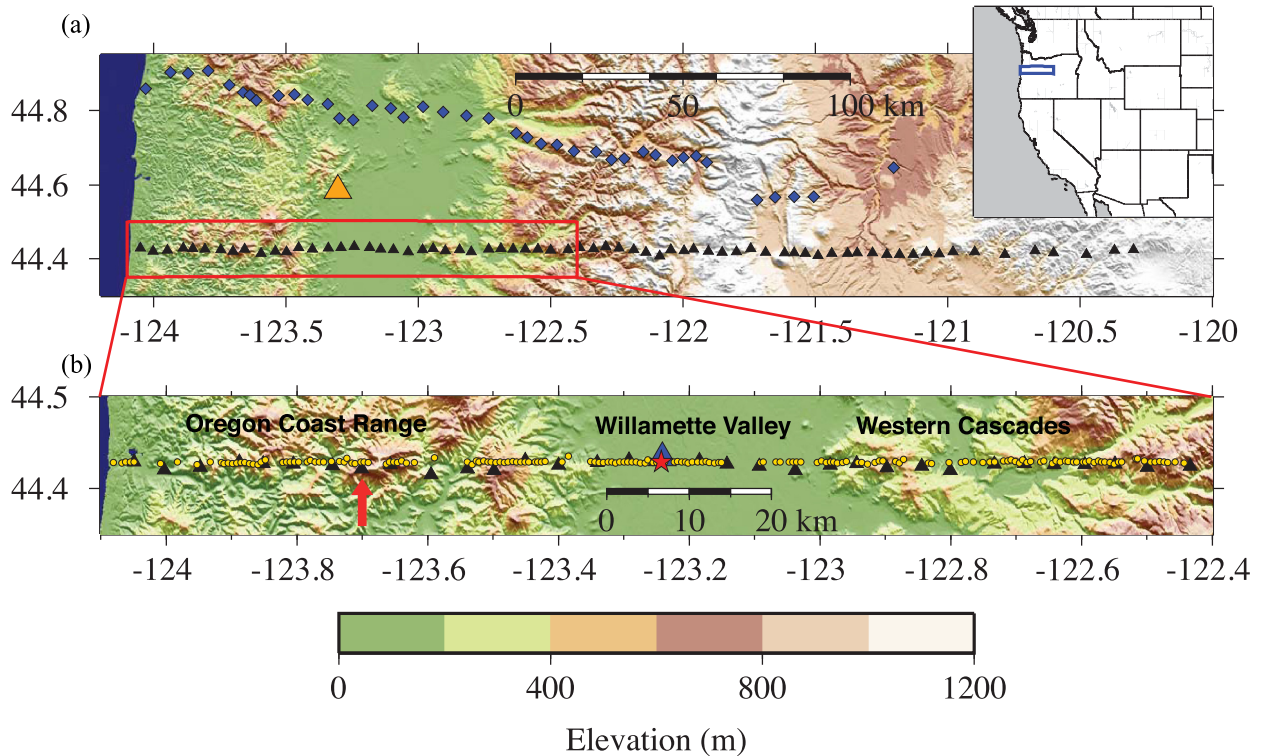
Figure 1. (a). The broad-band array CASC93 (black triangles) and MT survey array EMSL (Wannamaker *et al.* 2014) (blue diamonds) with topography shown in the background. The orange triangle is the broad-band station COR in the IU network. (b). The zoom in plot of the red box in (a). ZO2017 stations are shown as golden circles; the CASC93 stations are shown as black triangles. The red arrow points to a location at 30 km east of the shore which will be used as the example location in section 2.2. The blue triangle and red star are the source stations for the cross-correlation records shown in Fig. 3 for the CASC93 and ZO2017 arrays, respectively.

structure with receiver function analysis (Audet *et al.* 2010; Tauzin *et al.* 2017; Ward & Lin 2017), unanticipated longer period teleseismic surface wave signals up to 120 s period were recorded from teleseismic events (Fig. 2 and Supporting Information Fig. S1). The band-passed earthquake waveforms recorded by the geophones are highly consistent with those recorded by a nearby broad-band station (COR; orange triangle in Fig. 1a). The broad period range of the nodal instrument's sensitivity opens up the possibility of complementing existing broad-band data to investigate the detailed crustal structure with ambient noise tomography.

The Cascadia subduction zone is a 1000-km long plate boundary separating the oceanic Juan de Fuca and continental North American plates. In this study, we focused on the crustal structure of the top 24 km in the Cascadia forearc region in central Oregon. Three major physiographic provinces exist in our study region: the Oregon Coast Range, the Willamette Valley and the Western Cascades (Fig. 1b). The present-day central Oregon Cascadia forearc formed on the ocean floor until it was uplifted ∼12 Ma ago (Wells 2006). The basement of the forearc region is composed of the Siletzia terrane, which is an accumulation of submarine and subaerial oceanic basalt forming around 55–49 Ma and is interpreted to result from the Yellowstone hotspot passing over this part of the plate system (Mc-Crory & Wilson 2013; Wells *et al.* 2014). On top of the Siletzia basement, marine siltstone and sandstones were deposited in the forearc basin during the accretion of the Siletzia terrane that uplifted Western Oregon above sea level and created the Coast Range ∼12 Ma (Wells 2006). Further inland, subduction-related volcanic activity has produced in the Cascade Range since ∼40 Ma ago. The Western Cascades have not been volcanically active since ∼17 Ma and are

mainly composed of basalts and basaltic andesite representing the western flanks of the once wider volcanic arc. About 18–15 Ka ago, the Missoula glacial outburst floods filled the Willamette basin with silts and sands. In the lower-to-mid crust beneath the Willamette Valley, Wannamaker *et al.* (2014) observed a conductive region interpreted as subduction-related fluids migrating to crustal depths.

Since the double beamforming method was first proposed by Krüger *et al.* (1993, 1996) to analyse seismic asymmetric multipath effects and study inhomogeneity at the core–mantle boundary using nuclear sources, it has been used to image lower-mantle heterogeneities (Scherbaum *et al.* 1997), select and identify different body wave phases with synthetic data (Boué *et al.* 2013), enhance surface wave signals from ambient noise cross-correlations across the Transportable array (USArray; Boué *et al.* 2014) and identify and enhance body and surface waves from noise cross-correlations of dense geophone arrays (Nakata *et al.* 2016). In this study, we apply an array-based surface wave double beamforming tomography method to the ambient noise cross-correlations across the ZO2017 nodal and CASC93 linear arrays. Our tomography results reveal the slow velocity sediments in the Willamette basin at shallow depths (<6 km), the fast velocity basaltic Siletzia terrane at mid-to-lower crustal depths (>7 km) and a low-velocity anomaly beneath the Willamette valley (>15 km) likely associated with subduction-related fluid migration.

2 DATA AND METHODS

In this study, we used ambient noise data from two seismic arrays. One is the nodal geophone array ZO2017 (Ward *et al.* 2017; Fig. 1)
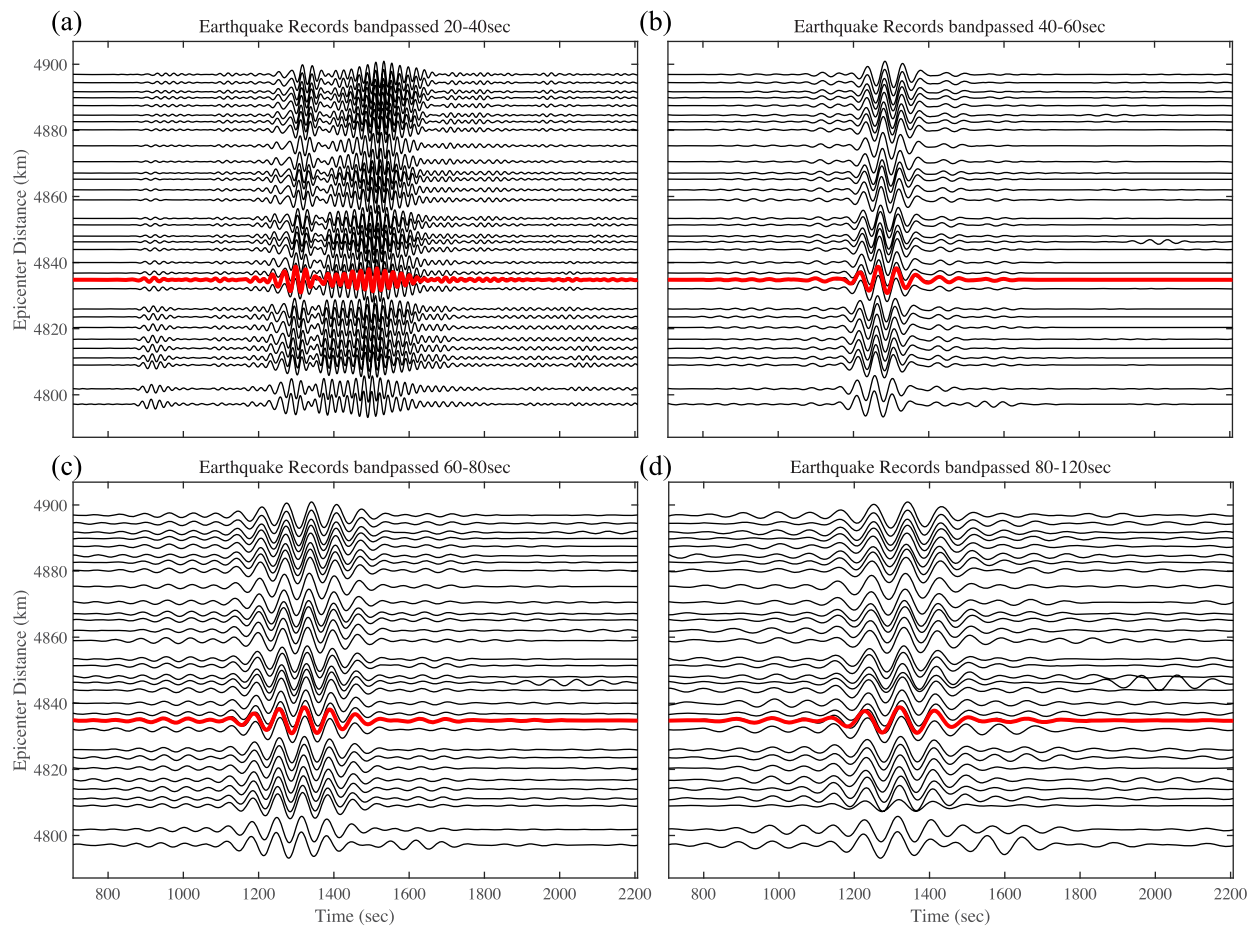
Figure 2. Rayleigh wave signals from the magnitude 7.7 earthquake at Komandorskiye Ostrova Region, Russia (54.47° N, 168.81° E) on 2017 July 17, recorded by the ZO2017 array (black) and a broad-band station COR (red), bandpassed at 20–40, 40–60, 60–80 and 80–120 s periods, respectively. No instrument response was removed from any of the traces. The location of the station COR is shown as an orange triangle in Fig. 1(a).

which consists of 174 three-component 5 Hz geophones deployed for about 40 d from 2017 June to August along an ~130 km west–east survey line. The array stretched from the west coast of Oregon to the Western Cascades with 500 m station spacing. The other seismic array is a three-component broad-band seismometer array CASC93 (Trehu *et al.* 1994; Rondenay *et al.* 2001; Fig. 1) that consists of 69 stations deployed for about a year from 1993 to 1994. The broad-band array is about 300 km long with ~5 km station spacing, along the same survey line as the nodal geophone array but extends further to the east.

2.1 Cross-correlations

We calculate ambient noise cross-correlations between each station pair for both ZO2017 and CASC93 arrays, respectively. The process of cross-correlation is similar to that described by Lin *et al.* (2013) but adapted for three-component noise data. First, the north-, east- and vertical-component noise data were cut into 1 hr segments and transformed to the frequency domain. Then the spectra of all three components were whitened equally based on the vertical component and 9-components cross-correlations were computed for each station pair. Next, the 1 hr 9-component cross-correlations were normalized equally by the maximum amplitude of the vertical–vertical cross-correlation after being transformed back into the time domain. All 1-hr normalized cross-correlations were then stacked to

obtain the final cross-correlations for each station pair. In this study, although we used multiple components of the cross-correlations to examine the particle motions of the surface waves, only vertical–vertical cross-correlations were used in our tomography results.

Fig. 3 shows the vertical–vertical cross-correlation record sections between a source station and all receiver stations for ZO2017 and CASC93 arrays, respectively. Clear fundamental Rayleigh waves were observed in the cross-correlations at 3–15 s periods and are highly asymmetric for all periods. For receiver stations on the east of the source station, the Rayleigh wave signals only exist on the positive time lags, while for receiver stations on the west of the source station, the signals only exist on the negative time lags. This indicates that almost all of the noise energy is from the west likely caused by the ocean–solid earth interaction (Hasselmann 1963) and/or counterpropagating ocean waves interaction (Longuet-Higgins 1950) near the Oregon coast. In the following analysis, we only used positive time lags of the cross-correlations of all west–east source–receiver pairs.

2.2 Double beamforming tomography

In this study, we develop a double beamforming method that utilizes the dense array configuration to enhance the signal while simultaneously directly measuring the surface wave phase velocities from
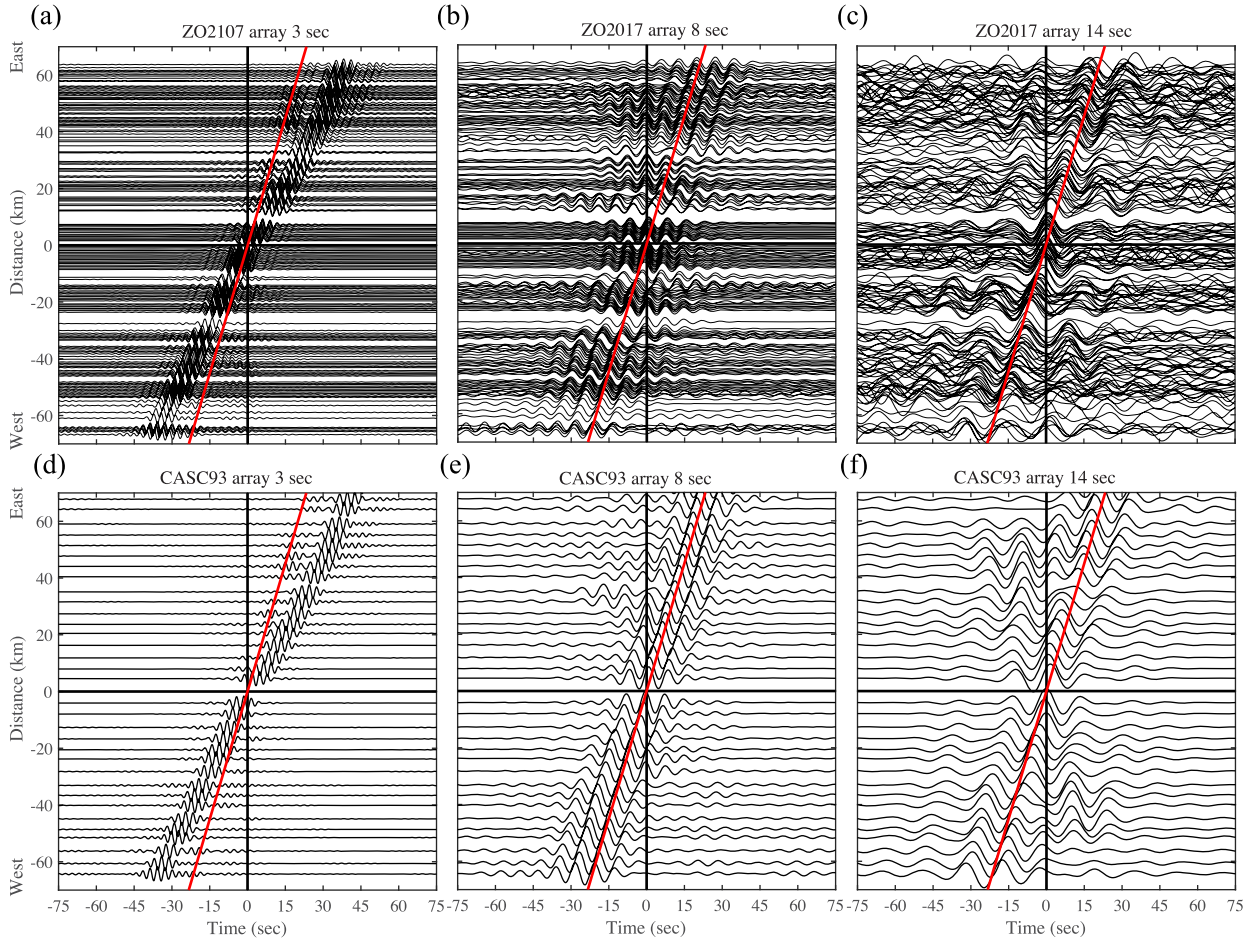
Figure 3. (a)–(c): Cross-correlation record sections calculated between a source nodal station (red star in Fig. 1) and all other ZO2017 array stations, bandpassed centred at 3, 8 and 14 s period. The red line is a reference line with 3.0 km s^{-1} velocity; (d)–(f): Same as the (a)–(c) but for the CASC93 array. The centre station is shown as a blue triangle in Fig. 1.

both ZO2017 and CASC93 arrays. The first step involves selecting the beam width (D) which controls the limitation of the lateral imaging resolution. Under the ray theory framework, we do not aim to resolve structures smaller than half of the selected wavelength (Wang & Dahlan 1995). Here we selected the beam width as half the wavelength for the ZO2017 array and required the beam width to be greater than 10 km for 3–5 s period and greater than 16 km for 6–9 s period. The minimum beam width threshold prevents too few stations from being used in the beam and ensures the number of waveforms is sufficient to produce robust results. For the CASC93 array, since the stations spacing is much larger than ZO2017, we used one wavelength as the beam width and the same period-dependent minimal beam width threshold.

For a source beam centred at Xs_c and a receiver beam centred at Xr_c, considering the beam width (D), the range of the source beam is $(Xs_c−D/2)$—$(Xs_c+D/2)$ and the range of the receiver beam is $(Xr_c−D/2)$—$(Xr_c+D/2)$. We use the cross-correlations between stations in the source beam and stations in the receiver beam, and band-passed these waveforms around a specific period (T). Note that a far-field criterion (Yao *et al.* 2006; Wang *et al.* 2017) was imposed to remove station pairs with distances shorter than 1 wavelength (at 6–15 s) and 1.5 wavelength (at 3–5 s). The slightly less strict criterion for long periods is to retain sufficient number of

cross-correlations for beamforming analysis. To only stack the fundamental Rayleigh waves, we set a period-dependent maximum velocity v_{max} (empirically determined as 2.0–4.7 km s for 3–15 s signals) and calculated a minimum arrival time $t_{min} = d/v_{max}$, where d is the interstation distance. The 0 s—t_{min} of the waveforms was cut out and t_{min} to $t_{min} + T/2$ was tapered with a cosine function. After the cutting and tapering, the waveforms were normalized by the maximum amplitude, shifted and stacked. This process affectively removes spurious precursor and higher mode signals. The stacked waveform in our analysis is calculated similar to eq. (1) in Nakata *et al.* (2016) but simplified for surface waves across a 1-D array:

$$Z\left(u_s, u_r, t\right) = \frac{1}{N_s N_r} \sum_{i=1}^{N_s} \sum_{j=1}^{N_r} z\left(s_i, r_j, t - \tau_s + \tau_r\right), \quad (1)$$

where Z is the stacked waveform, u_s and u_r are the Rayleigh wave phase slowness at the source and receiver sides, t is time lag, N_s and N_r are the number of stations within the source and receiver beams, respectively, and s_i and r_j represent the source and receiver stations. τ_s and τ_r are shift times which are defined as

$$\tau_s = \left(Xs_i − Xs_c\right) u_s, \quad (2)$$

and

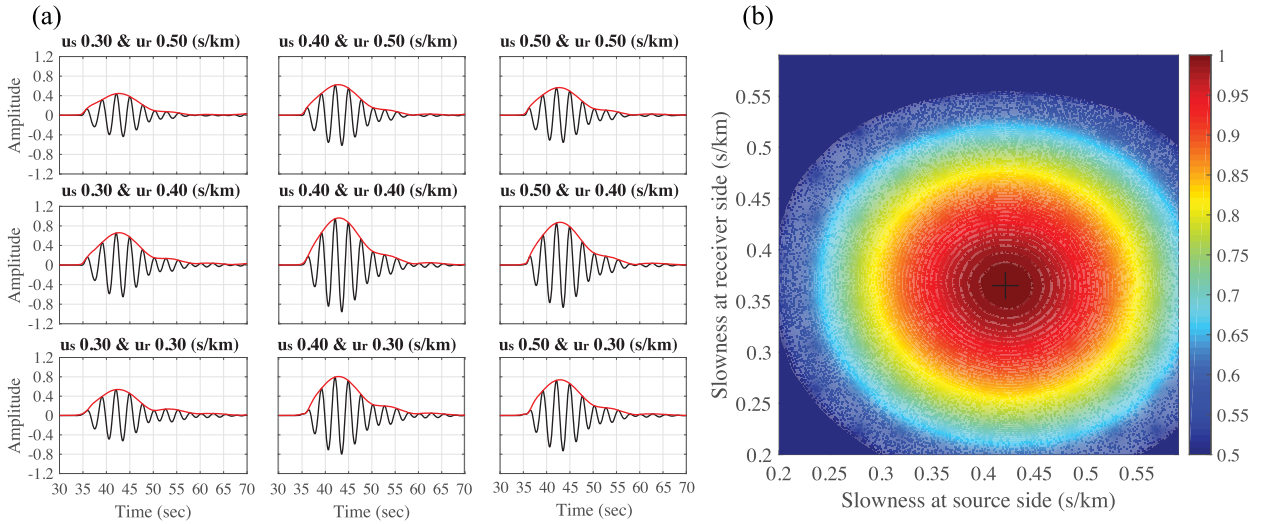$$\tau_r = \left(Xr_j − Xr_c\right) u_r, \quad (3)$$

Figure 4. (a) Stacked waveforms with different source beam slowness u_s and receiver beam slowness u_r. The u_s and u_r are shown on the titles of the subplots. (b) The maximum envelope amplitude of the stacked waveforms with respect to the source side slowness u_s and receiver side slowness u_r. The black cross marks the location with the maximum amplitude.
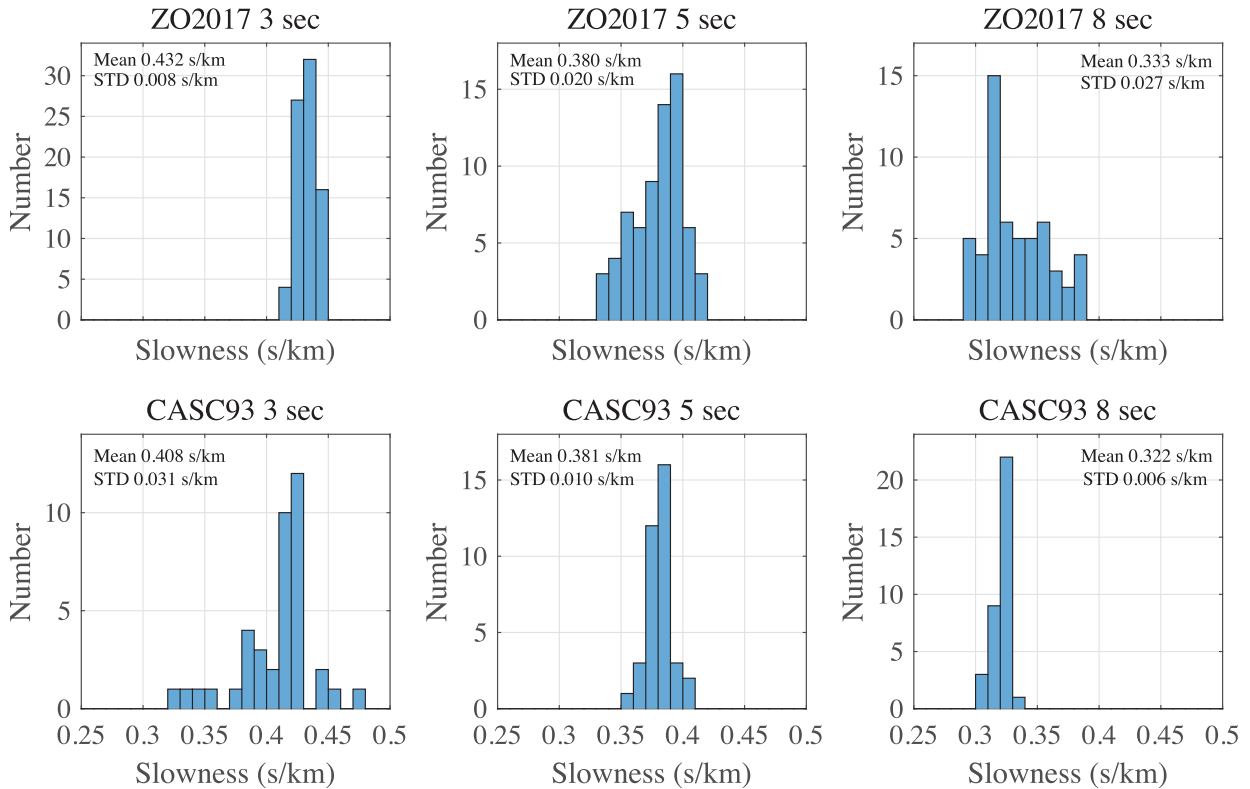

Figure 5. Histograms of the slowness measurements at 30 km east of the coast (red arrow in Fig. 1b) at 3, 5 and 8 s period for ZO2017 array (top) and CASC93 array (bottom).

where Xs_i and Xr_j are the location of the source station s_i and receiver station r_j. Here we assume there is no off-great-circle propagation. We note that the method can be expanded to spontaneously evaluate the direction of wave propagation in addition to the phase slowness with the presence of 2-D arrays.

Next, the envelope function of the stacked waveform was calculated:

$$A\left(u_s, u_r, t\right) = \left|\mathcal{H}\left(Z\left(u_s, u_r, t\right)\right)\right|, \qquad (4)$$

where A is the envelope function and $\mathcal{H}$ represents the Hilbert transform operator. Fig. 4 shows an example of the stacked cross-correlations with various different slowness for one source and receiver beam pair where the source beam centred at $X s_c = 30$ km (distance from the coast) and the receiver beam centred at $X r_c = 100$ km. If the u_s and u_r closely represent the slowness of the structure at the source and the receiver sides, the waveforms would stack constructively, and the stacked waveform would have the highest
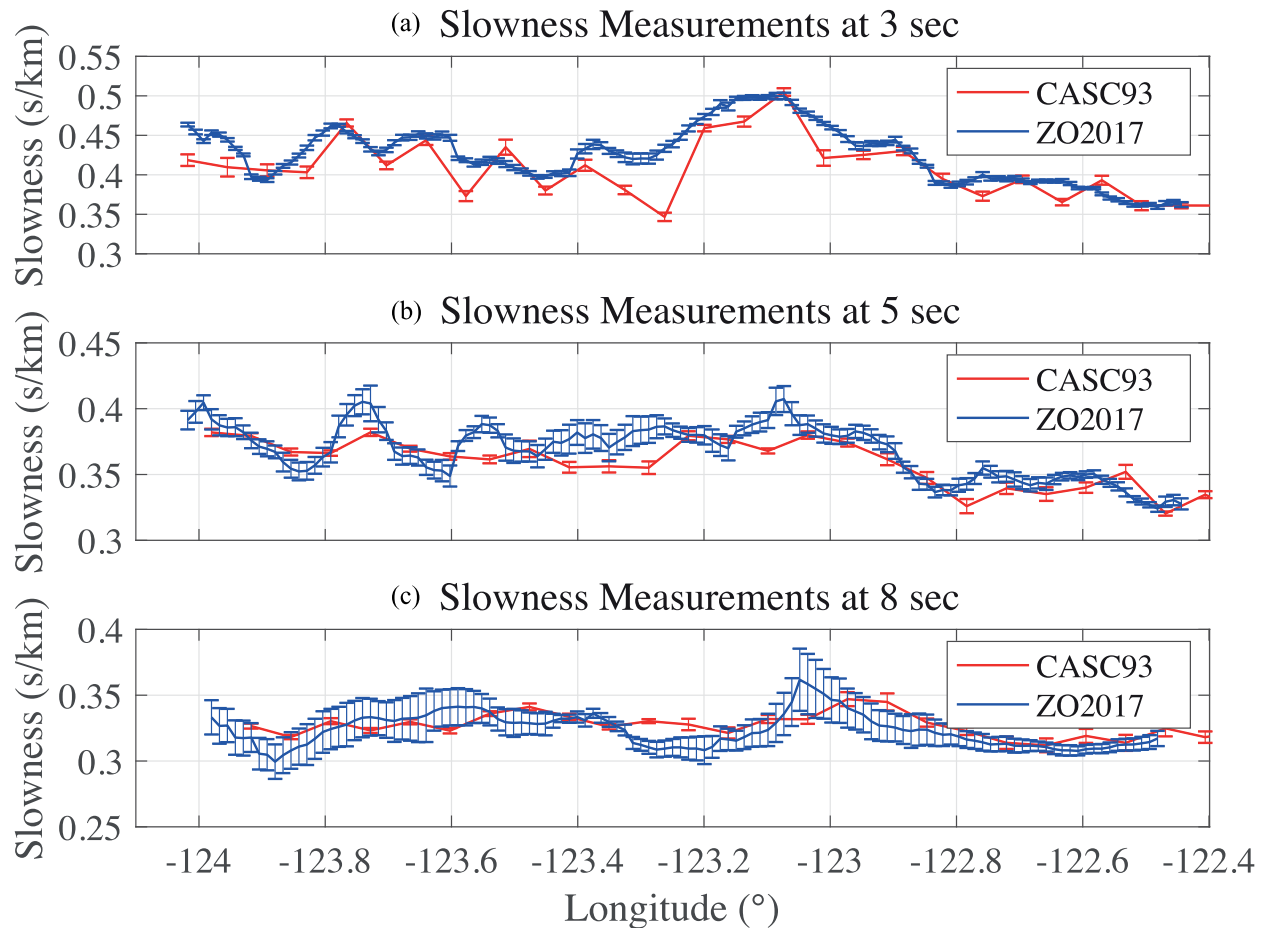
Figure 6. (a)–(c) Slowness measurements across the arrays at 3, 5 and 8 s period for the ZO2017 array (blue) and the CASC93 array (red). Error bars represent the uncertainties or standard deviation of the mean.

amplitude. To determine the best slowness, we performed a 2-D grid search looking for the maximum amplitude of the stacked envelope waveforms (Fig. 4b).

To repeatedly measure slowness and statically determine uncertainty, we moved the source beam and the receiver beam and repeat the double beamforming process. The source beam moves from the west end of the array to the east end of the array, and the receiver beam moved from the east of the source beam to the east end of the array, under the condition that the far-field criterions are satisfied. Given the station spacing for the two seismic arrays, the source and receiver beam movement increment is 1 km for the ZO2017 array and 5 km for the CASC93 array. By using all available source beam–receiver beam combinations, numerous slowness measurements can be obtained at each location across the array. The final slowness at a particular location is determined as the mean value of all the slowness measurements after removing extreme measurements beyond two standard deviations. The uncertainty is determined by the standard deviation of the mean, which is the standard deviation divided by the squared root of the number of independent measurements. Note that while we use overlapping beams to obtain all available slowness measurements, we determine the number of independent measurements based on the number of non-overlapping beams. To statistically obtain a mean slowness and uncertainty at a particular location, we require the number of measurements to be greater than 20 for the ZO2017 array data, and greater than 10 for the CASC93 array data.

Fig. 5 shows example histograms of the slowness measurements at a location 30 km east of the coast (red arrow in Fig. 1b) at 3, 5 and 8 s period for both the ZO2017 and CASC93 arrays. At 3 s period, we observe that the ZO2017 measurements are better constrained resulting in lower uncertainty estimates, whereas at longer periods, the CASC93 array data performs better. The short-period measurements are more robust for the ZO2017 array mostly due to the dense distribution of stations. The long-period measurements are more robust for the CASC93 array which might result from: (1) the CASC93 array being deployed for a longer time (1 yr) compared to the ZO2017 array (40 d), thus the Rayleigh waves have a higher signal/noise ratio and the noise source is more homogeneous; and/or (2) the broad-band stations having a stronger sensitivity to longer period signals, especially when the signal is relatively weak.

For each period, the mean slowness and its uncertainty at each location were used to construct phase slowness cross-sections across the entire line. Fig. 6 shows the slowness cross-sections at 3, 5 and 8 s period for both ZO2017 and CASC93 arrays. Then the slowness for all periods used in our study were combined and converted to 2-D phase velocity profiles for the two arrays (Fig. 7). The valid period ranges at each location for ZO2017 and CASC93 cross-sections are different due to the difference in array aperture and the requirement of minimal number of measurements mentioned in the previous paragraphs. We observe lower uncertainty estimates at shorter periods for the ZO2017 array and lower uncertainty estimates at longer periods for the CASC93 array. While a clear correlation can be
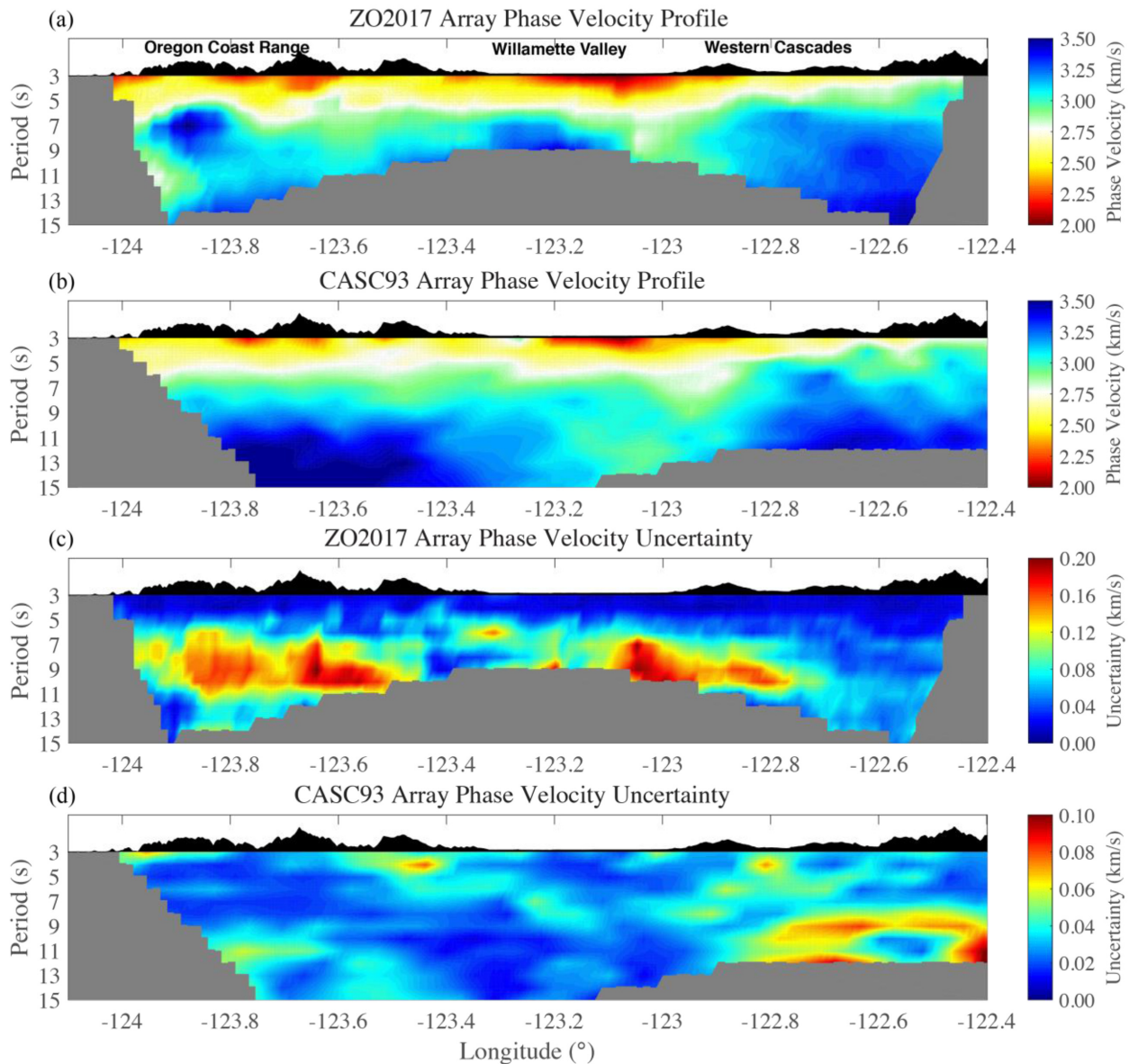
Figure 7. (a,b) Rayleigh wave phase velocity cross-sections and (c,d) uncertainties for the ZO2017 array and the CASC93 array.

observed between the nodal and broad-band slowness profiles, they differ in detail mostly due to differences in spatial resolution but also from differences in the noise distribution between the two experiments.

Comparing the velocity profiles (Fig. 7) from the two arrays, it can be noted that at short periods (<6 s) the velocity structure patterns are similar for the two data sets. At longer periods (>6 s), the uncertainties of the ZO2017 array profile increase significantly, and the reliability of the velocity structure degrades considerably. For example, the ellipse-shaped fast anomaly at 6–10 s period at −124.0 to −123.8 degrees is likely a spurious anomaly, given that it is not observed in the CASC93 array profile. We believe this bias is caused by the inhomogeneous noise source distribution. When the noise source direction is not parallel to the survey line, the velocity of the surface waves in the cross-correlations could be faster when compared to the homogenous noise distribution scenario (Lin *et al.* 2008; Yao & van der Hilst 2009). Although Rayleigh waves on the RR components are less sensitive to the inhomogeneity of noise

source distribution (Xu *et al.* 2018) and would be useful to correct for the bias, the Rayleigh waves on the RR components cross-correlations of the ZO2017 array are too weak to be observed for stations near the coast, particularly at longer periods (>6 s) likely due to the higher instrument/local noise observed in the horizontal components.

The bias due to an uneven source distribution is likely exacerbated at longer periods due to a wider stationary phase region, particularly for shorter distance interstation pairs (Snieder 2004). The fast velocity zone at 6–10 s period beneath the Willamette Valley in the ZO2017 array data is likely caused by the same reason. The ZO2017 array was only deployed for 40 d in the summer months, and the noise source distribution at 6–10 s period might be significantly off our survey line. On the contrary, the CASC93 array was deployed for a year, thus the year-averaged noise source would presumably distribute more homogenously than our nodal geophone data. Note that even for the CASC93 array data, the noise source is not expected to be completely homogenously distributed, and we expect
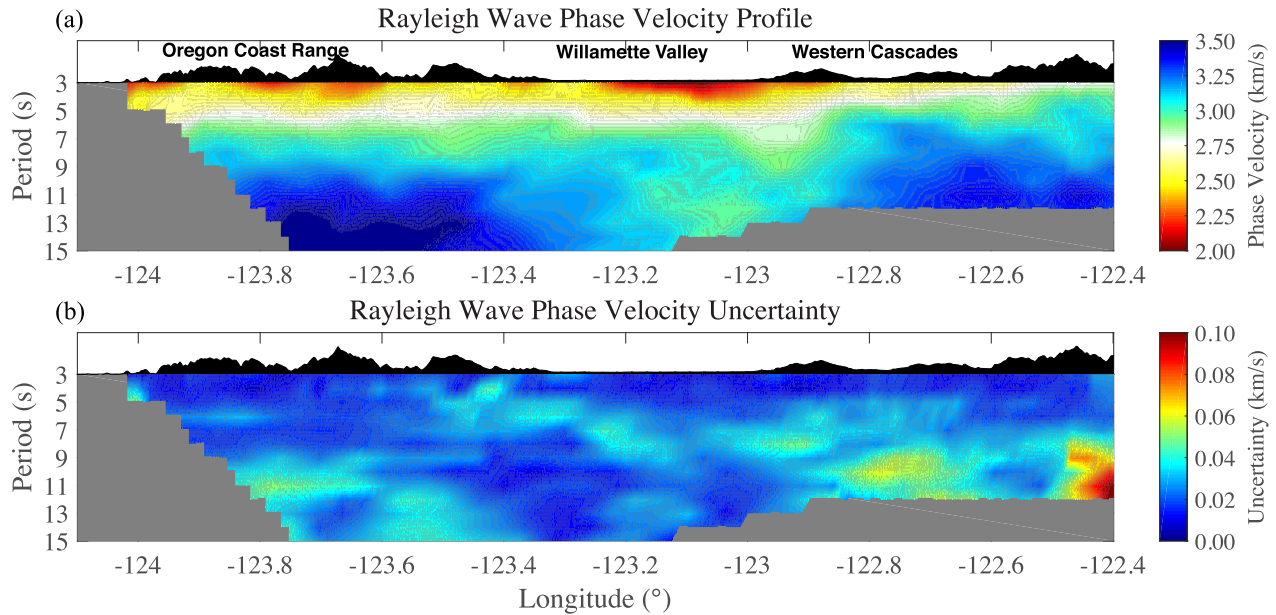
Figure 8. The combined Rayleigh wave phase velocity profile (a) and its uncertainty (b).

the velocity measurements at long periods near the coast to be less reliable resulting from its proximity to the dominant noise source.

To take the advantage of the complimentary information from the two different arrays, we combined the velocity profiles into a single profile. The velocity profiles were combined using the following weighted uncertainty averaging scheme:

$$c_m = \frac{1}{\left(\frac{1}{e_n{}^2} + \frac{1}{e_b{}^2}\right)} \left(\frac{1}{e_n{}^2} \cdot c_n + \frac{1}{e_b{}^2} \cdot c_b\right), \qquad (5)$$

where c_m is the combined phase velocity, e_n and e_b are the uncertainties of the nodal and broad-band measurements, c_n and c_b are the phase velocity measurements from nodal and broad-band arrays, respectively. At shorter periods (<6 s), if only c_n or c_b exists at a particular location and period, the combined velocity c_m equals to c_n or c_b. However, at longer periods (≥ 6 s), we required that c_b must exist to obtain a well-constrained c_m, given that the uncertainty estimates of the ZO2017 cross-section are considerably higher than that of the CASC93 cross-section. We calculated the uncertainty of c_m according to the theory of uncertainty propagation:

$$e_m = \sqrt{\frac{e_n{}^2 e_b{}^2}{e_n{}^2 + e_b{}^2}}. \qquad (6)$$

The combined phase velocity profile and uncertainties are presented in Fig. 8.

3 2-D SHEAR WAVE VELOCITY MODEL RESULTS

To obtain the shear wave velocity structure across the study area, we performed an iterative least-squares 1-D inversion across the Rayleigh wave phase velocity profile (Herrmann 2013). At each location, we started with a constant 1-D velocity model and calculated a penalty function that consists of the uncertainty-weighted misfit between the predicted and observed Rayleigh wave dispersion measurements and a regularization function of the model. Next, we perturbed the shear velocity model to decrease the penalty function and used the perturbed model as an updated starting model for

the next iteration. As the *Vs* was updated in each iteration, *Vp* and density were updated according to a fixed *Vp/Vs* ratio (1.75) and an empirical relationship between density and *Vp* (Brocher 2005). After 10 iterations, we found that the results tend to stabilize and stopped the iterative inversion process. This inversion workflow was performed at each location to obtain a series of 1-D shear wave velocity models (e.g. Fig. 9). Then the 1-D models were combined into a 2-D shear wave velocity profile (Fig. 10a).

Two 1-D *Vs* models located within the Oregon Coast Range and the Willamette Valley are shown in Fig. 9(a) as representative examples from our model. At most periods, the predicted Rayleigh wave phase velocity dispersion curve is within the uncertainty estimates of the data (Fig. 9c). The shallow slow velocity observed at the Willamette Valley location is expected and matches the sedimentary nature of the basin. Rayleigh wave phase velocity sensitivity kernels for the 1-D model at the Coast Range location are shown in Fig. 9(b). In order to define the resolvable depth range of the velocity profile, we calculated the Rayleigh wave sensitivity kernel of the longest available period at each location, then used the depth where the amplitude is 30 per cent of the peak amplitude as the cut-off depth. This is an arbitrary threshold but note a different threshold (e.g. 50 per cent) does not affect our final velocity model significantly and our interpretations remain unchanged.

4 DISCUSSION

4.1 Synthesis with regional geology, receiver function analysis, electric resistivity measurements and previous velocity models

We observe a strong correlation between the resolved velocity structures in our results (Fig. 10a) and the surface geology. For example, at shallow depths (<4 km), the Oregon Coast Range region, which is dominated by the Tyee Formation, is relatively slow corresponding to the accreted Middle Eocene marine deposits. The Willamette Valley consists of Quaternary alluvial and lacustrine deposits and
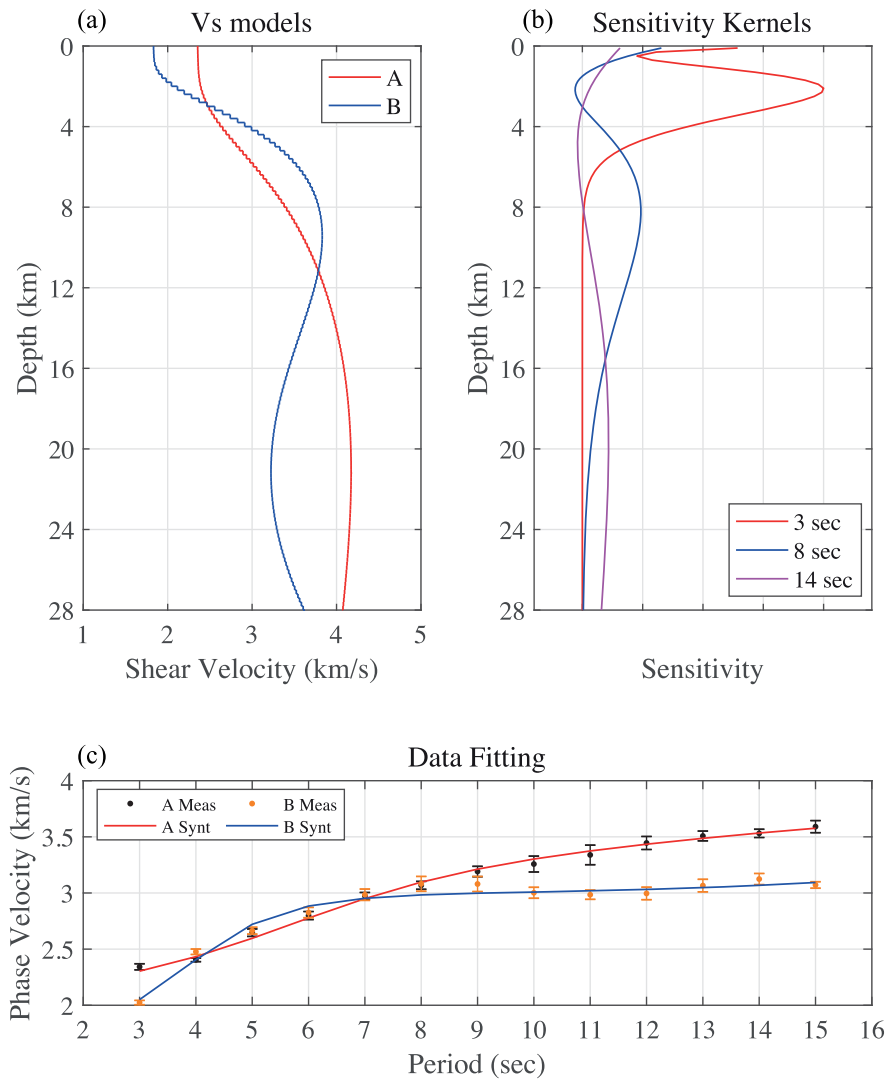
Figure 9. (a) 1-D shear velocity models at 30 km (location A; Coast Range) and 75 km (location B; Willamette Valley) east of the shore (red reverse triangles in Fig. 10a). (b) Sensitivity kernels of the Rayleigh waves at 3, 8 and 14 s period based on the *Vs* model at location A. (c). Rayleigh wave phase velocity measurements and predicted dispersions based on the 1-D *Vs* models in (a). Error bars represent uncertainties time 2.

is resolved in our model as a prominent slow anomaly. Further inland to the Western Cascades region, the sedimentary layer becomes thinner eastwards. The resolved shallow crustal structures are also consistent with a recent receiver function study (Fig. 10a; Ward *et al.* 2018). Depth migrated 4.8 Hz (Gaussian 'a' value of 10) receiver functions from a stack of two teleseismic events (Magnitude 6.3 & 7.7, both on 2017 July 17 and at Komandorskiye Ostrova Region, Russia) are plotted on top of our 2-D *Vs* velocity profile in Fig. 10(a). Topography and ray geometry of the incoming teleseismic waves have been accounted for in the receiver function migrations. The first non-zero positive peaks in the migrated receiver functions at 1–5 km depth likely represents the interface between the sedimentary layer or unweathered/unaltered Siletzia terrane. We refer the readers to Ward *et al.* (2018) for additional information on the receiver function analysis across the ZO2017 geophone array.

At greater depths (>7 km), fast velocities are observed in the Oregon Coast Range and Western Cascades, representing the Siletzia terrane basement composed of submarine and subaerial oceanic basalt. The Rayleigh wave phase velocity measurements and shear

wave model derived in this study, besides the enhanced resolution, are overall consistent with previous studies based on the continental scale USArray Transportable Array (e.g. Lin *et al.* 2008 and Lin *et al.* 2014; see Supporting Information Fig. S2 for comparison). Beneath the Willamette Valley, a robust low-velocity anomaly is observed with the top starting as shallow as 8 km but on average ∼10 km and extending through our models depth resolution. A zone of low electrical resistivity at a similar longitude but north of our line (∼50 km) was observed by a previous magnetotelluric study (Figs 1a and 10b; Wannamaker *et al.* 2014). The cause of this conductive region was suggested as fluids released from the subducting slab that have migrated to the lower crust. Although the magnetotelluric (MT) and seismic (*Vs*) results are not from the same spatial line, we suggest the slow anomaly we observe in our shear velocity profile correlates with the same feature seen in the MT survey, likely corresponding to a regional scale feature. Note that the slow anomaly in the velocity profile does not mirror the low resistivity area exactly. Two possible reasons for the discrepancy between the two cross-sections include: (1) The two lines are ∼50 km away from
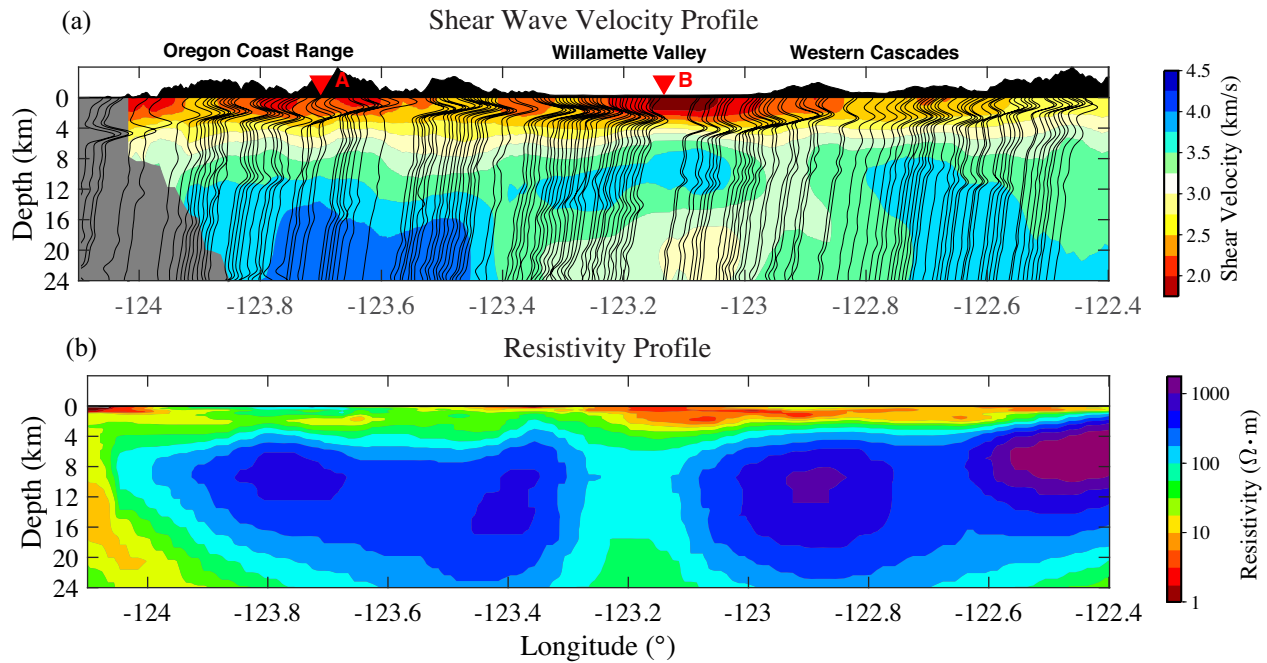
Figure 10. (a). The inverted 2-D shear wave velocity profile. The receiver functions across the ZO2017 array from the stack of a magnitude 7.7 event and a magnitude 6.3 event both at Komandorskiye Ostrova Region earthquake on 2017 July 17 (Ward *et al.* 2018) are shown as the thin grey lines. The two inverted red triangles show the example locations used in Fig. 9. The topography is vertically exaggerated by 4:1. (b). The resistivity profile along the blue diamond survey line shown in Fig. 1(a) (Wannamaker *et al.* 2014). Note, although the two lines are offset by ∼50 km, there are first-order similarities between the two cross-sections.

each other, thus the geometry of the cross-sections of the anomaly body might be different; and (2) Each method is sensitive to a different physical Earth property and might not mirror each other one to one. Work-in-progress includes a 3-D MT inversion in the area that will hopefully be available soon and provide a more meaningful direct comparison (Egbert *et al.* 2017).

4.2 Collocated cross-correlations comparison between ZO2017 and CASC93 arrays

Due to the natural corner frequency of the instruments, the signals observed by geophones are expected to gradually deteriorate with the increase of period compared to broad-band stations. To evaluate the data quality from the geophone array beyond its instrument corner frequency (5 Hz), we directly compared the cross-correlations for the almost collocated station pairs (geophone and broad-band stations located within 1 km) between ZO2017 and CASC93 arrays. We calculated cross-correlations for the CASC93 array with the data from June to August in 1993 (the same deploying months as the ZO2017 array) to avoid potential bias due to the seasonal noise source variation. The process to obtain cross-correlations is the same as described in section 2.1. The locations of the station pairs are shown in Fig. 11(a), and the cross-correlation waveforms are shown in Fig. 11(b). While the cross-correlation waveforms are overall consistent across the entire period band, the Rayleigh wave signals from the ZO2017 array have significantly smaller signal-to-noise ratios (SNR; Lin *et al.* 2008) above 9 s period (Fig. 11d). Phase velocity and group velocity dispersions of the Rayleigh waves are measured with Frequency–Time Analysis as described by Bensen *et al.* (2007) and Lin *et al.* (2008). Reflecting the SNR variation, the phase and group velocities for the two arrays are consistent between 3 and 8 s periods but not between 9 and 15 s periods. The

long-period Rayleigh waves from ZO2017 array are clearly less reliable compared to the CASC93 array, which is also the main reason why the ZO2017 array data have significantly higher uncertainties at long periods (>6 s) in Fig. 7.

4.3 Advantages and limitations

The double beamforming method we applied utilizes the dense array configuration to enhance weak but coherent signals and allows local phase velocities to be reliably measured. This is particularly important for long period noise cross-correlations across the nodal array where the signal-to-noise ratio can be poor (Fig. 3c). The exclusion of an inversion process to measure phase velocities avoids the degradation of velocity anomalies and the trade-off between regularization and misfit. In addition, the uncertainties of local phase velocities can be statistically estimated using repeated measurements from different receiver–source beam pairs, and the resolution of the tomography can be provided by the beam width.

We also demonstrate the potential bias in velocity measurement across the nodal array due to an inhomogeneous noise source distribution. This is particularly problematic for long-period measurements, which are more sensitive to the exact noise source distribution when the ray paths are short. While it remains to be shown, we suspect this issue can be mitigated by expanding the array aperture to increase the overall ray path distances. Another possibility to better account for the inhomogeneous noise source distribution is by deploying a 2-D dense array. Although we only apply the double beamforming method to linear arrays in this paper, the method can be easily modified and applied to gridded arrays. Thus, the double beamforming method can be an important complement to current seismic array tomography methods and have the exclusive virtue of effectively utilizing signals with low signal-to-noise ratios.
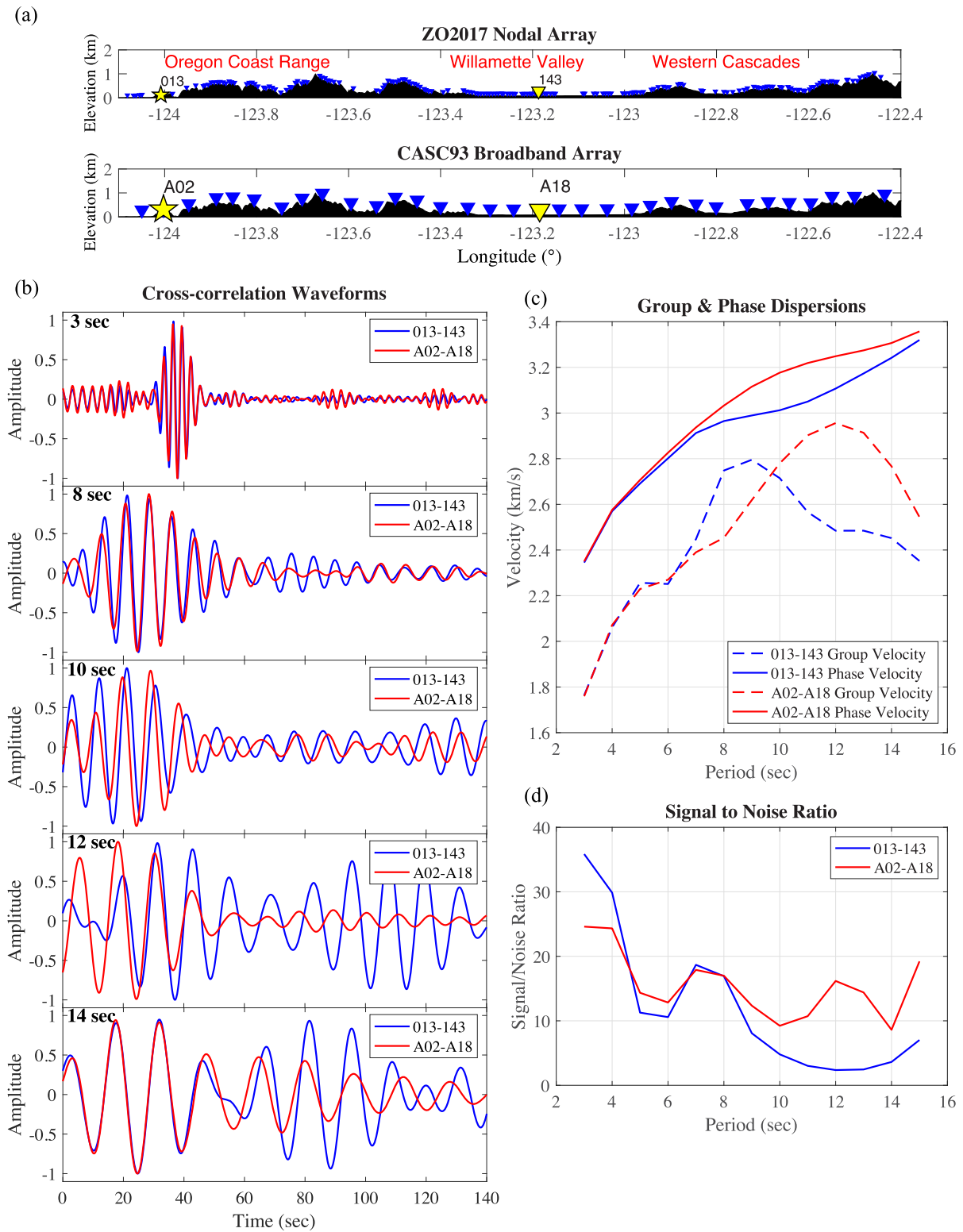
Figure 11. Collocated station pairs comparison. (a) Station maps for ZO2017 and CASC93 arrays. The blue triangles represent stations. The yellow stars and yellow triangles are source and receiver stations of the cross-correlations used in panel (b), respectively; (b) Cross-correlations waveforms for the two collocated station pairs at 3, 8, 10 and 14 s periods. The amplitudes are normalized separately for the two data sets; (c) Group and phase velocity dispersions for the two collocated station pairs; (d) Signal-to-noise ratios for the two collocated station pairs.

5 CONCLUSIONS

In this study, we show that the ambient noise double beamforming tomography method combined with a dense linear seismic array can be used to study detailed crustal structures on a regional scale. In particular, the availability of inexpensive and easy-to-deploy nodal geophone sensors now provides reduced deployment costs compared to conventional broad-band deployments and opens up new array configurations that complement traditional broad-band experiments. For this specific deployment, the 174 geophones were deployed in less than 5 d by two teams (2 d had only one team). However, lessons learned from this deployment could reduce that deployment time even further. Despite the 5 Hz corner frequency, the nodal instruments can reliably record broad-band seismic signals up to 120 s provided the signals are strong enough. We show clear Rayleigh wave signals between 3 and 15 s period can be extracted from the noise cross-correlations across the ZO2017 nodal array. Compatible signals can also be extracted using noise cross-correlations across the CASC93 broad-band array, which allows us to invert for detailed crustal structure to a greater depth. Our 2-D shear velocity model is consistent with what is expected from the regional geological setting. In the middle to lower crust, high-velocity anomalies can be associated with the basaltic Siletzia terrane, with a low-velocity anomaly observed beneath the Willamette Valley being associated with subduction zone fluids penetrating the mid-to-lower crust.

REFERENCES

Adams, A., Nyblade, A. & Weeraratne, D., 2012. Upper mantle shear wave velocity structure beneath the East African plateau: evidence for a deep, plateauwide low velocity anomaly, *Geophys. J. Int.,* **189,** 123–142.

Audet, P., Bostock, M.G., Boyarko, D.C., Brudzinski, M.R. & Allen, R.M., 2010. Slab morphology in the Cascadia fore arc and its relation to episodic tremor and slip, *J. geophys. Res.,* **115,** 1–15.

Bensen, G.D., Ritzwoller, M.H., Barmin, M.P., Levshin, A.L., Lin, F.-C., Moschetti, M.P., Shapiro, N.M. & Yang, Y., 2007. Processing seismic ambient noise data to obtain reliable broad-band surface wave dispersion measurements, *Geophys. J. Int.,* **169,** 1239–1260.

Bostock, M.G., Hyndman, R.D., Rondenay, S. & Peacock, S.M., 2002. An inverted continental moho and serpentinization of the forearc mantle, *Nature,* **417,** 536–538.

Boué, P., Roux, P., Campillo, M. & de Cacqueray, B., 2013. Double beamforming processing in a seismic prospecting context, *Geophysics,* **78,** V101–V108.

Boué, P., Roux, P., Campillo, M. & Briand, X., 2014. Phase velocity tomography of surface waves using ambient noise cross correlation and array processing, *J. geophys. Res.,* **119,** 519–529.

Brocher, T.M. 2005. Empirical relations between elastic wavespeeds and density in the Earth's crust, *Bull. seism. Soc. Am.,* **95**(6), 2081–2092.

Egbert, G.D., Yang, B., Bedrosian, P., Kelbert, A., Key, K., Livelybrooks, D., Parris, B.A. & Schultz, A., 2017. Three-dimensional magnetotelluric imaging of the cascadia subduction zone with an amphibious array, in *American Geophysical Union, Fall Meeting 2017, abstract #T42C-05,* Am. Geophys. Un., Washington DC.

Ekström, G., 2014. Love and Rayleigh phase-velocity maps, 5–40 s, of the western and central USA from USArray data, *Earth planet. Sci. Lett.,* **402,** 42–49.

Friedrich, W., 1998. Wave–theoretical inversion of teleseismic surface waves in a regional network: phase velocity maps and a three—dimensional upper-mantle shear-wave velocity model for southern Germany, *Geophys. J. Int.,* **132**(1), 203–225.

Hasselmann, K., 1963. A statistical analysis of the generation of microseisms, *Rev. Geophys.,* **1,** 177–210.

Herrmann, R.B., 2013. Computer programs in seismology: an evolving tool for instruction and research, *Seismol. Res. Lett.,* **84,** 1081–1088.

Krüger, F., Weber, M., Scherbaum, F. & Schlittenhardt, J., 1993. Doublebeam analysis of anomalies in the core-mantle boundary region, *Geophys. Res. Lett.,* **20,** 1475–1478.

Krüger, F., Scherbaum, F., Weber, M. & Schlittenhardt, J., 1996. Analysis of asymmetric multipathing with a generalization of the double-beam method, *Bull. seism. Soc. Am.,* **86,** 737–749.

Levshin, A.L., Ritzwoller, M.H., Barmin, M.P., Villaseñor, A. & Padgett, C.A., 2001. New constraints on the arctic crust and uppermost mantle: surface wave group velocities, *Pn*, and *Sn*, *Phys. Earth planet. Inter.,* **123,** 185–204.

Levshin, A.L., Barmin, M.P., Ritzwoller, M.H. & Trampert, J., 2005. Minorarc and major-arc global surface wave diffraction tomography, *Phys. Earth planet. Inter.,* **149,** 205–223.

Lin, F.-C., Ritzwoller, M.H., Townend, J., Bannister, S. & Savage, M.K., 2007. Ambient noise Rayleigh wave tomography of New Zealand, *Geophys. J. Int.,* **170,** 649–666.

Lin, F.C., Moschetti, M.P. & Ritzwoller, M.H., 2008. Surface wave tomography of the western United States from ambient seismic noise: Rayleigh and Love wave phase velocity maps, *Geophys. J. Int.,* **173,** 281–298.

Lin, F.-C., Li, D., Clayton, R.W. & Hollis, D., 2013. High-resolution 3D shallow crustal structure in Long Beach, California: application of ambient noise tomography on a dense seismic array, *Geophysics,* **78,** Q45–Q56.

Lin, F.-C., Tsai, V.C. & Schmandt, B., 2014. 3-D crustal structure of the western United States: application of Rayleigh-wave ellipticity extracted from noise cross-correlations, *Geophys. J. Int.,* **198**(2), 656–670.

Longuet-Higgins, M.S., 1950. A theory of the origin of microseisms, *Philos. Trans. R. Soc. A Math. Phys. Eng. Sci.,* **243,** 1–35.

McCrory, P.A. & Wilson, D.S., 2013. A kinematic model for the formation of the Siletz-Crescent forearc terrane by capture of coherent fragments of the Farallon and Resurrection plates, *Tectonics,* **32,** 718–736.

Nakata, N., Boué, P., Brenguier, F., Roux, P., Ferrazzini, V. & Campillo, M., 2016. Body and surface wave reconstruction from seismic noise correlations between arrays at Piton de la Fournaise volcano, *Geophys. Res. Lett.,* **43**(3), 1047–1054.

Prindle, K. & Tanimoto, T., 2006. Teleseismic surface wave study for *S*-wave velocity structure under an array: Southern California, *Geophys. J. Int.,* **166,** 601–621

Ritzwoller, M.H. & Levshin, A.L., 1998. Eurasian surface wave tomography: group velocities, *J. geophys. Res.,* **103,** 4839–4878.

Ritzwoller, M.H., Shapiro, N.M., Barmin, M.P. & Levshin, A.L., 2002. Global surface wave diffraction tomography, *J. geophys. Res. Solid Earth,* **107,** ESE 4-1–ESE4-13.

Rondenay, S., Bostock, M.G. & Shragge, J., 2001. Multiparameter two-dimensional inversion of scattered teleseismic body waves 3. Application to the Cascadia 1993 data set, *J. geophys. Res.,* **106,** 30 795–30 807.

Roux, P., Moreau, L., Lecointre, A., Hillers, G., Campillo, M., Ben-Zion, Y., Zigone, D. & Vernon, F., 2016. A methodological approach towards high-resolution surface wave imaging of the san jacinto fault zone using ambient-noise recordings at a spatially dense array, *Geophys. J. Int.,* **206,** 980–992.

Scherbaum, F., Krüger, F. & Weber, M., 1997. Double beam imaging: mapping lower mantle heterogeneities using combinations of source and receiver arrays, *J. geophys. Res.,* **102,** 507, doi:10.1029/96JB03115.

Shapiro, N.M., Campillo, M., Stehly, L. & Ritzwoller, M.H., 2005. High-resolution surface wave tomography from ambient seismic noise, *Science,* **307,** 1615–1618.

Snieder, R., 2004. Extracting the Green's function from the correlation of coda waves: a derivation based on stationary phase, *Phys. Rev. E. Stat. Nonlin. Soft Matter Phys.,* **69,** 046610, doi:10.1103/PhysRevE.69.046610.

Tauzin, B., Reynard, B., Perrillat, J.P., Debayle, E. & Bodin, T., 2017. Deep crustal fracture zones control fluid escape and the seismic cycle in the Cascadia subduction zone, *Earth planet. Sci. Lett.,* **460,** 1–11.

Trehu, A.M., Asudeh, I., Brocher, T.M., Luetgert, J.H., Mooney, W.D., Nabelek, J.L. & Nakamura, Y., 1994. Crustal architecture of the cascadia forearc, *Science,* **266,** 237–243.

Trampert, J. & Woodhouse, J.H., 2003. Global anisotropic phase velocity maps for fundamental mode surface waves between 40 and 150 s, *Geophys. J. Int.,* **154,** 154–165.

Wang, Y., Lin, F.-C., Schmandt, B. & Farrell, J., 2017. Ambient noise tomography across Mount St. Helens using a dense seismic array, *J. geophys. Res.,* **122,** 4492–4508.

Wang, Z. & Dahlen, F.A., 1995. Validity of surface-wave ray theory on a laterally heterogeneous earth, *Geophys. J. Int.,* **123,** 757–773.

Wannamaker, P.E., Evans, R.L., Bedrosian, P.A., Unsworth, M.J., Maris, V. & McGary, R.S., 2014. Segmentation of plate coupling, fate of subduction fluids, and modes of arc magmatism in Cascadia, inferred from magnetotelluric resistivity, *Geochem. Geophys. Geosyst.,* **15,** 4230–4253.

Ward, K.M., 2015. Ambient noise tomography across the southern Alaskan Cordillera, *Geophys. Res. Lett.,* **42,** 3218–3227.

Ward, K.M. & Lin, F., 2017. On the viability of using autonomous three-component nodal geophones to calculate teleseismic *Ps* receiver functions with an application to old faithful, yellowstone, *Seismol. Res. Lett.,* **88,** 1268–1278.

Ward, K.M., Porter, R.C., Zandt, G., Beck, S.L., Wagner, L.S., Minaya, E. & Tavera, H., 2013. Ambient noise tomography across the Central Andes, *Geophys. J. Int.,* **194,** 1559–1573.

Ward, K.M., Lin, F., Kiser, E.D., Thomas, A.M. & Schmandt, B., 2017. *Central Oregon Dense 3C Node Transect: International Federation of Digital Seismography Networks,* Other/Seismic Network, doi:10.7914/SN/ZO_2017.

Ward, K.M., Lin, F. & Schmandt, B., 2018. High-resolution receiver function imaging across the Cascadia Subduction Zone using a dense nodal array, *Geophys. Res. Lett.,* **45**(22), 12 218–12 225.

Wells, R., 2006. Oregon Geology - Parent of the soil, foundation for the vine. USGS No. 2006-1069.

Wells, R., Bukry, D., Friedman, R., Pyle, D., Duncan, R., Haeussler, P. & Wooden, J., 2014. Geologic history of Siletzia, a large igneous province in the Oregon and Washington Coast Range: correlation to the geomagnetic polarity time scale and implications for a long-lived Yellowstone hotspot, *Geosphere,* **10,** 692–719.

Xu, Z., Dylan Mikesell, T. & Gribler, G., 2018. Source-distribution estimation from direct Rayleigh waves in multicomponent crosscorrelations, in *SEG Technical Program Expanded Abstracts 2018. August 2018, 3090–3094,* SEG, Tulsa.

Yao, H., Van Der Hilst, R.D. & ,De Hoop, M.V., 2006. Surface wave array tomography in SE Tibet from ambient seismic noise and two-station analysis - I. Phase velocity maps, *Geophys. J. Int.,* **166,** 732–744.

Yao, H., Beghein, C. & Van Der Hilst, R.D., 2008. Surface wave array tomography in SE Tibet from ambient seismic noise and two-station analysis - II. Crustal and upper-mantle structure, *Geophys. J. Int.,* **173,** 205–219.

Yao, H. & van der Hilst, R.D., 2009. Analysis of ambient noise energy distribution and phase velocity bias in ambient noise tomography, with application to SE Tibet, *Geophys. J. Int.,* **179,** 1113–1132.

Zigone, D., Ben-Zion, Y., Campillo, M. & Roux, P., 2015. Seismic tomography of the Southern California plate boundary region from noise-based Rayleigh and love waves, *Pure appl. Geophys.,* **172,** 1007–1032.

SUPPORTING INFORMATION

Supplementary data are available at *GJI* online.

Figure S1. Earthquake event waveforms recorded by the ZO2017 array (black) and the broad-band station COR (red), bandpassed at 20–40 s periods. (a) Waveforms from an M6.6 event on 2017 July 11 at Auckland Islands, N.Z. Region ∼12 500 km away from the array. (b). Waveforms from an M5.8 event on 2017 July 6 at Montana, U.S. ∼900 km away from the array. No instrument response was removed from any of the traces. The location of the station COR is shown as an orange triangle in Fig. 1(a). No clear signal is observed at periods longer than 40 s for the two events.

Figure S2. Phase velocity and shear velocity results compared with previous studies. (a) Phase velocity profile. (b) Phase velocity model from Lin *et al.* (2008). (c) Shear velocity profile. (d) Shear velocity model from Lin *et al.* (2014).

Please note: Oxford University Press is not responsible for the content or functionality of any supporting materials supplied by the authors. Any queries (other than missing material) should be directed to the corresponding author for the paper.